MATERIALS SCIENCE

Phase transition enhanced superior elasticity in freestanding single-crystalline multiferroic $BiFeO_3$ membranes

Bin Peng[1]*, Ren-Ci Peng[1]*, Yong-Qiang Zhang[2]*, Guohua Dong[1]*, Ziyao Zhou[1†], Yuqing Zhou[3], Tao Li[3†], Zhijie Liu[4], Zhenlin Luo[4], Shaohao Wang[5], Yan Xia[6], Ruibin Qiu[1], Xiaoxing Cheng[7], Fei Xue[7], Zhongqiang Hu[1], Wei Ren[1], Zuo-Guang Ye[8], Long-Qing Chen[7], Zhiwei Shan[2], Tai Min[3], Ming Liu[1†]

The integration of ferroic oxide thin films into advanced flexible electronics will bring multifunctionality beyond organic and metallic materials. However, it is challenging to achieve high flexibility in single-crystalline ferroic oxides that is considerable to organic or metallic materials. Here, we demonstrate the superior flexibility of freestanding single-crystalline $BiFeO_3$ membranes, which are typical multiferroic materials with multifunctionality. They can endure cyclic 180° folding and have good recoverability, with the maximum bending strain up to 5.42% during in situ bending under scanning electron microscopy, far beyond their bulk counterparts. Such superior elasticity mainly originates from reversible rhombohedral-tetragonal phase transition, as revealed by phase-field simulations. This study suggests a general fundamental mechanism for a variety of ferroic oxides to achieve high flexibility and to work as smart materials in flexible electronics.

INTRODUCTION

Flexible electronics is booming for foldable and wearable electronic devices, i.e., electronic skins, health monitoring systems, and human-machine interfaces (*1*, *2*). Ferroic oxides are essential building blocks of various electronic devices due to their excellent dielectric, ferroelectric, and piezoelectric properties (*3*). Among them, multiferroic oxides distinguish themselves by their unique multiferroic properties and will bring multifunctionality to flexible electronics such as sensing and actuation (*4*, *5*), energy storage capacitors (*6*), memories, and logic devices (*7*). Flexible electronics require their components to have superior flexibility or elasticity to conform to various curved surfaces or complicated bent conditions. However, bulk ferroic and multiferroic oxides are always thought to be inherently brittle because of the strong covalence/ionic bond and lack of dislocation glide planes as compared to organic or metallic materials that could easily withstand large bending strain up to tens of percent (*8*, *9*). Therefore, the realization of superior flexibility in ferroic oxides, especially multiferroic oxides, will greatly promote their application in flexible electronics.

With the reduction of dimensionality, some brittle oxides have exhibited unexpected flexibility that is different from their bulk counterparts. This is much obvious in oxide nanowires with a high surface-to-volume ratio, in which surface elasticity plays a dominant role through surface relaxation and reconstruction (*10*). Except for nanowires, two-dimensional ferroic oxides are much more plausible for device integration in flexible electronics. Currently, the widely studied flexible ferroic oxide thin films are those deposited on flexible mica (*11*), but their flexibility is limited by the mica substrate, the applied bending strain in those previous studies is always below 1%, and their superior elasticity is not explored. The advancement in fabricating strategies of freestanding single-crystalline ferroic oxide membranes provides useful platforms to study their intrinsic mechanical deformation behavior (*12*, *13*). In ferroelectric/ferroelastic oxides, polarization rotation and the accompanying ferroelastic domain switching are important ways to accommodate strong strain/stress (*14*). Recently, we reported that the freestanding single-crystalline $BaTiO_3$ membranes could endure a giant bending strain up to 10% without any crack or damage (*15*). This superior elasticity originated from continuous polarization dipole rotations rather than conventional 90° domain switching (*15*).

Moreover, phase transition in oxides offers strong atomic displacement tolerance and induces additional strain that exceeds the elasticity limit of bulk materials. For example, zirconia micro-pillars exhibited super-elasticity, benefiting from both martensitic phase transition and size reduction (*16*). In ferroic oxides, the phase transition is also a general phenomenon to accommodate large strain/stress or generate large piezostrain. Electric field–induced phase transition could induce two to three times strain than the linear piezoelectric response in relaxor ferroelectric single crystals (*17*). In strained thin films, e.g., $BiFeO_3$ epitaxial thin film, the phase transition could be induced by large misfit strain (*7*, *18*, *19*) or mechanical stress (*20*, *21*). Typically, rhombohedral $BiFeO_3$ epitaxial thin films could transform to the tetragonal phase under a biaxial compressive strain up to over 4.5% (*18*). However, the explored strain level in

[1]Electronic Materials Research Laboratory, Key Laboratory of the Ministry of Education, School of Electronic and Information Engineering, Center for Spintronics and Quantum System, State Key Laboratory for Mechanical Behavior of Materials, Xi'an Jiaotong University, Xi'an 710049, China. [2]Center for Advancing Materials Performance from the Nanoscale (CAMP-Nano) and Hysitron Applied Research Center in China (HARCC), State Key Laboratory for Mechanical Behavior of Materials, Xi'an Jiaotong University, Xi'an 710049, China. [3]Center for Spintronics and Quantum System, State Key Laboratory for Mechanical Behavior of Materials, School of Materials Science and Engineering, Xi'an Jiaotong University, Xi'an, Shaanxi 710049, China. [4]National Synchrotron Radiation Laboratory, University of Science and Technology of China, Hefei 230026, China. [5]Department of Microelectronics Science and Technology, Fuzhou University, Qi Shan Campus, Fuzhou 350108, China. [6]College of Physics and Information Engineering, Fuzhou University, Fuzhou 350108, China. [7]Department of Materials Science and Engineering, Pennsylvania State University, University Park, PA 16802, USA. [8]Department of Chemistry and 4D LABS, Simon Fraser University, Burnaby, BC V5A 1S6, Canada.
*These authors contributed equally to this work.
†Corresponding author. Email: ziyaozhou@xjtu.edu.cn (Z.Z.); taoli66@xjtu.edu.cn (T.L.); mingliu@xjtu.edu.cn (M.L.)

bulk is still below 1 to 2%, and larger strain achieved in thin films is at the nanoscale and clamped by the substrates. The enhancement of flexibility in freestanding single-crystalline ferroic oxide membranes by combined ferroelasticity and phase transition remains unexplored.

In this study, we choose freestanding single-crystalline $BiFeO_3$ membranes as the prototype to study its mechanical deformation behavior and corresponding fundamental mechanism. $BiFeO_3$ is a typical multiferroic material that has ferroelectricity, ferroelasticity, (anti)ferromagnetism, and magnetoelectric coupling among those ferroic orders (*4*, *7*, *18*). In $BiFeO_3$ epitaxial thin films deposited on rigid substrates, their phase and domain are highly sensitive to the misfit strain between the films and the substrates (*7*, *18*, *19*). Moreover, freestanding single-crystalline $BiFeO_3$ thin films also exhibited extraordinary ferroelectricity even down to one unit cell, while the mechanical properties were not studied (*13*). Here, we fabricated freestanding single-crystalline $BiFeO_3$ membranes with >100 nm thickness and examined their mechanical deformation behavior under large bending strain far beyond 1%. Unexpectedly, it can withstand cyclic 180° folding and has good recoverability, with the smallest radius of curvature about 1 μm. The underlying mechanism for freestanding $BiFeO_3$ membranes to accommodate a large bending strain up to 5.42% without any crack or damage is analyzed by phase-field simulation.

RESULTS

Preparation of freestanding $BiFeO_3$ membranes

The fabrication of freestanding single-crystalline $BiFeO_3$ membranes started from an epitaxial growth of $BiFeO_3/Sr_3Al_2O_6$ heterostructure on $SrTiO_3$(001) substrates (see Materials and Methods), followed by a water etching process to fully release $BiFeO_3$ thin films from the substrates, and ended by a transferring process that moves freestanding $BiFeO_3$ membranes onto any other substrates (Fig. 1A). In the beginning, $Sr_3Al_2O_6$ was chosen as a sacrificial layer during epitaxial film growth because it is water-soluble and its lattice matches well with $BiFeO_3$, enabling the fabrication of large-scale freestanding perovskite membranes (*12*, *13*). The epitaxy of $SrTiO_3$(001)/$Sr_3Al_2O_6$/$BiFeO_3$ heterostructures was confirmed by both x-ray diffraction (Fig. 1B) and cross-sectional transmission electron microscopy (TEM) image (Fig. 1C). Benefiting from very small lattice mismatch (only 0.03%) between $Sr_3Al_2O_6$ [a = 15.844 Å; (*12*)] and $BiFeO_3$ ($4 \times a_{pc}$ = 15.84 Å), only (00l) diffraction peak could be observed, and $Sr_3Al_2O_6$(00l) and $BiFeO_3$(00l) diffraction

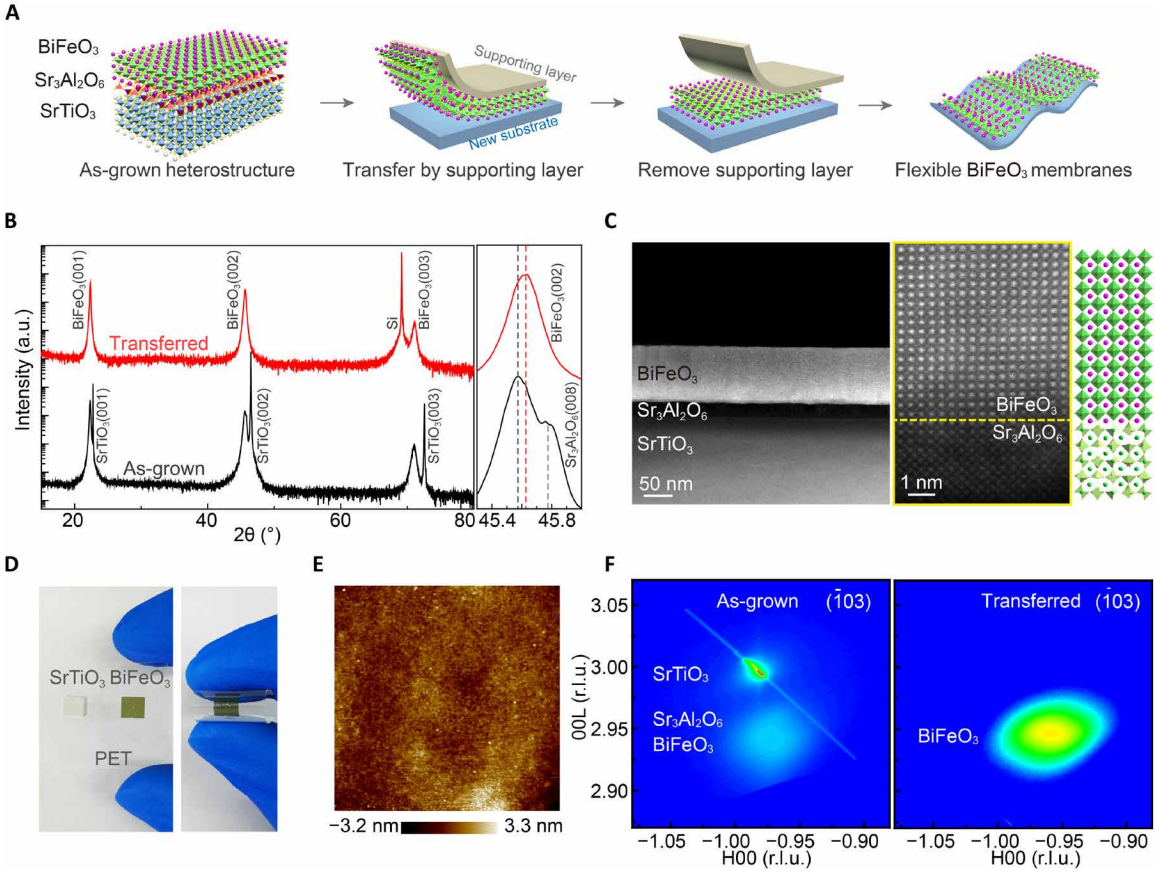

Fig. 1. Synthesis of freestanding single-crystalline $BiFeO_3$ membranes. (**A**) Schematics of the whole fabrication process: growing $BiFeO_3/Sr_3Al_2O_6$ heterostructure on $SrTiO_3$ substrates, releasing $BiFeO_3$ films from the substrates by water etching, and then transferring $BiFeO_3$ membranes to any other substrates. (**B**) X-ray diffraction patterns of as-grown $SrTiO_3$(001)/$Sr_3Al_2O_6$/$BiFeO_3$ heterostructure and transferred $BiFeO_3$ membranes on the silicon substrate. a.u., arbitrary units. (**C**) Cross-sectional TEM and HAADF-STEM image of an $SrTiO_3$(001)/$Sr_3Al_2O_6$/$BiFeO_3$ heterostructure. (**D**) Optical images of a 5 mm–by–5 mm $BiFeO_3$ membrane that transferred to polyethylene terephthalate (PET) and exhibited good flexibility. Photo credit: Bin Peng, Xi'an Jiaotong University. (**E**) Surface morphology of transferred $BiFeO_3$ on PDMS by AFM. (**F**) RSM of $BiFeO_3$ film around (−103) peak before (left) and after (right) releasing from the substrate. r.l.u., reciprocal lattice units.

peaks are very close to each other. Their atomic-scale microstructure was examined by cross-sectional high-angle annular dark-field (HAADF) imaging using scanning TEM (STEM) (Fig. 1C), and the interface between $Sr_3Al_2O_6$ and $BiFeO_3$ is sharp and clear.

Before releasing $BiFeO_3$ thin films, a soft supporting layer was coated or attached on the surface of $SrTiO_3/Sr_3Al_2O_6/BiFeO_3$ heterostructures, and they were then immersed in deionized water to separate $BiFeO_3$ from the substrates (Fig. 1A; see also Materials and Methods). Freestanding $BiFeO_3$ membranes could then be transferred onto any other substrates by removing the supporting layer, or the supporting layer itself serves as the flexible substrate (Fig. 1A; see also Materials and Methods). Here, millimeter-scale (5 mm by 5 mm) freestanding $BiFeO_3$ membranes were fully released from $SrTiO_3$ substrates to a commercial transparent screen protector sheet (Fig. 1D) or oxidized silicon substrates (fig. S1), and the freestanding $BiFeO_3$ membranes transferred to soft supporting layer exhibit high flexibility (Fig. 1D). The freestanding $BiFeO_3$ membranes have smooth surfaces and low surface roughness of 0.55 nm, observed by atomic force microscopy (AFM) (Fig. 1E). The transferred $BiFeO_3$ membranes maintain their single crystallinity as that of the as-grown ones. Representative reciprocal space mapping (RSM) of as-grown $SrTiO_3/Sr_3Al_2O_6/BiFeO_3$ heterostructure and transferred $BiFeO_3$ membranes on Si are shown in Fig. 1F, and here, RSMs around the (−103) peak are presented. The lattice constant for $Sr_3Al_2O_6$ was 15.828 Å, a little smaller than its bulk value due to the clamping of $SrTiO_3$ substrates. The lattice constant of $BiFeO_3$ thin films decreased from 3.9847 to 3.9804 Å after releasing from the substrate (Fig. 1B) due to the disappearance of the substrate clamping effect.

The single crystallinity of freestanding $BiFeO_3$ membranes was confirmed again by plane-view STEM. Here, typical plane-view STEM images of thin freestanding $BiFeO_3$ membranes were presented (Fig. 2A). It was in a folded state and had good electron transparency, supported by a holey carbon TEM grid. Totally folded two-dimensional perovskite thin films down to few unit cells thick were observed before (*13*); here, the folded $BiFeO_3$ membranes are much thicker than that, highlighting the high flexibility of freestanding $BiFeO_3$ membranes. Figure 2B shows an atomic-resolution HAADF-STEM image. This "Z-contrast" image presents two distinct atom columns: The larger one with high intensity are Bi atoms, and the smaller one with low intensity are Fe atoms. It is also clear that Fe atoms deviate from the center of the unit cell. Those features match well with the rhombohedral perovskite structure. The selected-area electron diffraction pattern shown in Fig. 2C reveals that the lattice constant is a = 3.974 Å and β = 89.5°, very close to that of the bulk $BiFeO_3$. The ferroelectricity and local polarization switching of the freestanding $BiFeO_3$ membranes were demonstrated by piezoelectric force microscopy (PFM) (Fig. 2, D to F). Here, a box-in-box switched domain pattern was written on the transferred $BiFeO_3$ membranes by applying ±8 V (Fig. 2, D and E), where the inner and outer boxes indicated polarization up and down states, respectively. Typical local PFM amplitude and phase hysteresis loops are presented (Fig. 2F), and they are quite symmetric and no imprint was observed that is suitable for ferroelectric memories. In addition, both the as-grown $SrTiO_3/Sr_3Al_2O_6/BiFeO_3$ heterostructure and the transferred $BiFeO_3$ membrane exhibited ferromagnetic behaviors at room temperature (fig. S2).

Flexibility of freestanding $BiFeO_3$ membranes

Freestanding single-crystalline $BiFeO_3$ membranes are mechanically robust and exhibit super-elastic behavior under a large bending strain without any crack or damage. Figure 3 shows the in situ scanning electron microscopy (SEM) observation of bending the freestanding $BiFeO_3$ membranes. A nanoribbon was cut from freestanding $BiFeO_3$ membranes by focused ion beam (FIB) and then handled by nanomanipulator tips in SEM. One tip was used to hold the nanoribbon, and another was used to push the nanoribbon to bend (Fig. 3A). The lateral size of this nanoribbon was 17 μm (length) by 4 μm

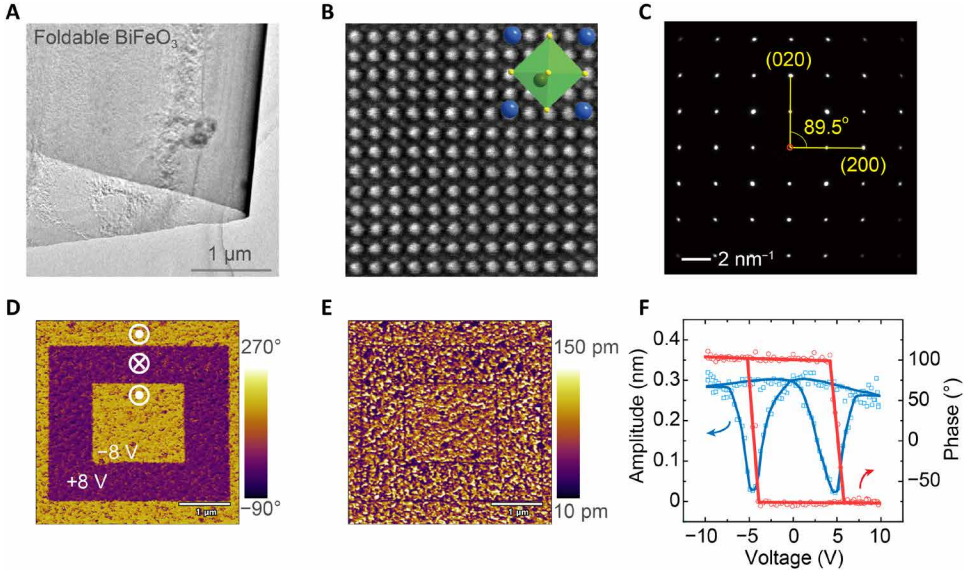

Fig. 2. Microstructure and ferroelectricity of freestanding single-crystalline $BiFeO_3$ membranes. (**A**) Plane-view HAADF-STEM images of a freestanding $BiFeO_3$ membrane in a folded state, supported by Cu grid with lacey carbon film. (**B**) Atomic-resolution HAADF-STEM image from the top view and shift of Fe^{3+} cations from the center of oxygen octahedron are clear. (**C**) Corresponding selected-area electron diffraction pattern of freestanding $BiFeO_3$ membrane. (**D**) Phase and (**E**) amplitude response mapping of a box-in-box domain pattern written by PFM under ±8 V. (**F**) Typical amplitude and phase hysteresis loops (solid lines are guide for the eyes).

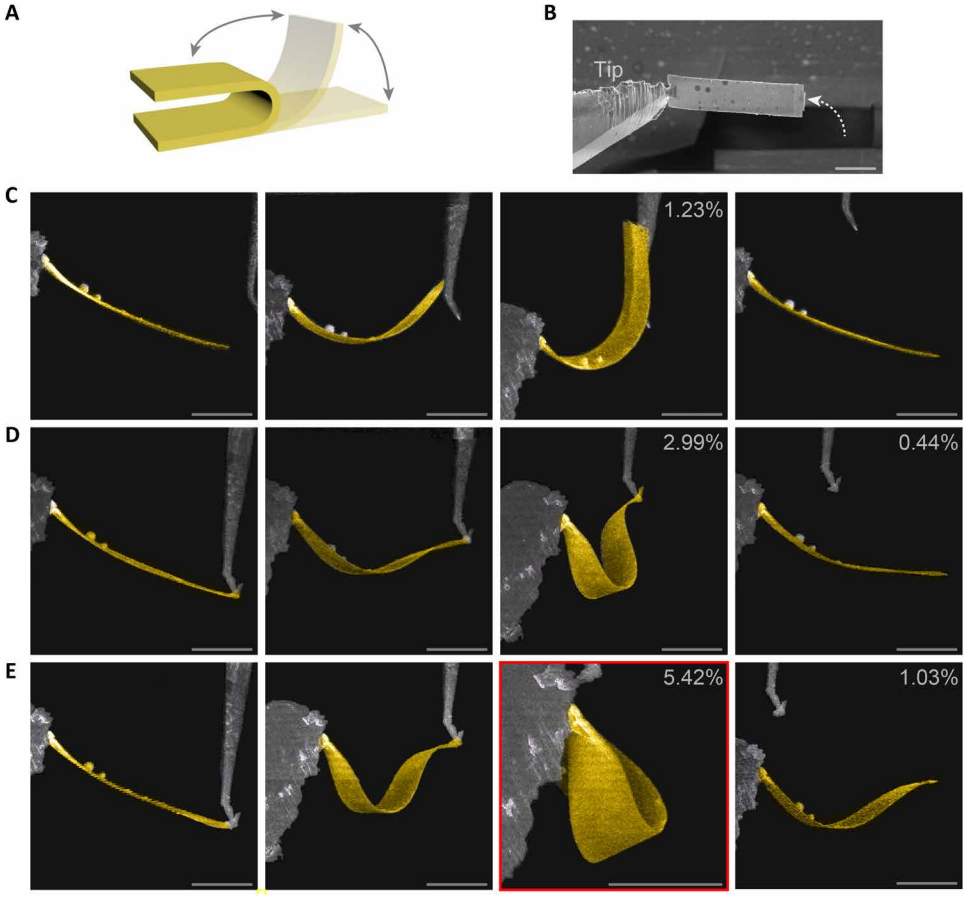

Fig. 3. In situ SEM observation of bending the freestanding $BiFeO_3$ membranes. (**A**) Schematics of in situ bending a nanoribbon. (**B**) A $BiFeO_3$ nanoribbon cut by FIB with one side fixed to a tip, and this nanoribbon has a size of 17 μm (length) by 4 μm (width) by 110 nm (thickness). (**C** to **E**) Several runs of in situ bending-unbending test. The first column shows the initial state during each run of bending, the second column shows the reducing of the radius of curvature during bending, and the third column exhibits the minimum radius of curvature at each run. The maximum bending strain reaches 1.23, 2.99, and 5.42%, corresponding to the third column of (C) to (E). During in situ bending test, the largest bending strain reaches 5.42% without any break or crack, and the corresponding panel was marked in red. The fourth column of (C) to (E) shows the final state of the nanoribbon after unbending at each run, with the residual strain of about 0, 0.44, and 1.03%, respectively. Scale bars, 5 μm (B to E).

(width) (Fig. 3B) with a thickness of about 110 nm, which was confirmed from the depth profile of AFM (fig. S3) and cross-sectional TEM (Fig. 1C) images. This nanoribbon was bent-unbent for several runs (Fig. 3, C to E), and the videos were recorded and shown in movies S1 to S3. Here, we present typical images that were captured from the videos, including the initial, intermediate, maximum, and residual bending states of each run. For the first run, this nanoribbon was bent to a maximum strain of about 1.23% (for calculations, see table S1), and it recovered immediately to the initial state once the pushing tip was removed (Fig. 3C). The recovering process is so quick that we could not observe a continuous change in the video. In Fig. 3C, the moving tip was not fixed to the nanoribbon. To ensure applied larger force, the moving tip was then fixed to the other side of the nanoribbon at the initial state for the following runs. For the second run (Fig. 3D), the maximum bending strain reaches 2.99%. However, after removing the pushing tip, the nanoribbon could not recover to its initial state but has a small residual strain of 0.44%. When we push the nanoribbon to a 180° fold state, both ends touched each other and the maximum bending strain increased to 5.42% (Fig. 3E). After removing the pushing tip, the nanoribbon had a larger residual strain of 1.03%. After that, the nanoribbon was bent again (fig. S4), with the maximum bending strain of about 2.74%. Unexpectedly, with the removal of the pushing tip, the residual strain still maintained 1.02%, which was commensurate with that shown in Fig. 3E.

Figure 3 demonstrates the high flexibility and recoverability of freestanding single-crystalline $BiFeO_3$ membranes, and it is natural to wonder why they have super-elasticity that could endure at least 5.42% bending strain. Although such deformation behavior seems to be induced by classic ferroelastic domain switching, lattice strain in rhombohedral perovskite induced by ferroelastic domain switching is usually less than 0.5% (*22*, *23*) and mechanical stress–induced strain from combined ferroelastic domain switching and elastic deformation is still below 1% in bulk rhombohedral perovskite (*24*, *25*). By contrast, tetragonal perovskites always have a large spontaneous strain ($c/a - 1$), which is far beyond 1%. $BiFeO_3$ epitaxial thin films are highly sensitive to lattice mismatch strain, and a biaxial compressive strain exceeding 4.5% will induce phase transition from the rhombohedral phase to the tetragonal phase (*7*, *18*). Therefore, it is very likely that the phase transition is responsible for the super-elasticity in freestanding $BiFeO_3$ membranes. As the mechanical boundary condition in previous theoretical calculations

is different from our case (*18*), the previously predicted phase diagram may not be suitable for our freestanding $BiFeO_3$ membranes.

Phase-field simulation of mechanical bending of $BiFeO_3$ membranes

Furthermore, phase-field simulations are performed to reveal the dynamic evolution of $BiFeO_3$ ferroelectric nanodomains and the behavior of phase transition between rhombohedral (R) $BiFeO_3$ and tetragonal (T) $BiFeO_3$ in the $BiFeO_3$ membranes upon bending or unbending. The initial domain state of freestanding $BiFeO_3$ membranes without bending is R1+ single domain [i.e., its polarization direction of (1 1 1) as shown in Fig. 4A within a simulated size of 800 nm (length) by 2 nm (width) by 110 nm (thickness)]. In Fig. 4B, the two-dimensional distribution of the polarization vectors within $BiFeO_3$ membranes upon bending is obtained by starting from R1+ domain as the initial state and applying a bending angle (θ) of 30.56°, which corresponds to a maximum strain of −3.67% at the bottom surface (or +3.67% at the top surface). There exists an R-T mix-phase in the bent membrane (where the volume fraction of T phase is ~4.46%) in Fig. 4B. The fact that T phase (i.e., c+ domain) only appears at the bottom, which is a highly compressive region, and R phase (i.e., R1+ domain) in the tensile strained region reveals that the polarization orientation (or the phase state) is related to the strain state. Unlike the sharp boundary from the conventional R-T mix-phase observed in the system of the $BiFeO_3$ film/substrate (*7*, *18*, *26*, *27*), the phase boundary between T phase and R phase is a rather thicker transitional region where polarization rotates continuously from c+ domain to R1+ domain, possibly arising from both the relaxed elastic strain to decrease the elastic energy at this specific mechanical boundary and the local flexoelectric field (*28*–*30*) from strain gradient for the bending state of the $BiFeO_3$ film. Also, the magnitude of the polarization increases continuously from the bottom to the top surface along the *z* axis for all bent cases shown in the left panels of Fig. 4 (B to D), resulting from the strain state with a gradient variation. Figure 4C shows that the fraction of c+ domain or T phase increases to 19.23% when the bending angle θ reaches 45.84°.

In Fig. 4F, the maximum strain of the $BiFeO_3$ membranes upon bending is proportional to the bending angle of the film. Also, during the recovery process of the membrane upon unloading, as the bending angle (θ) decreases from 45.84° to 9.17°, the phase

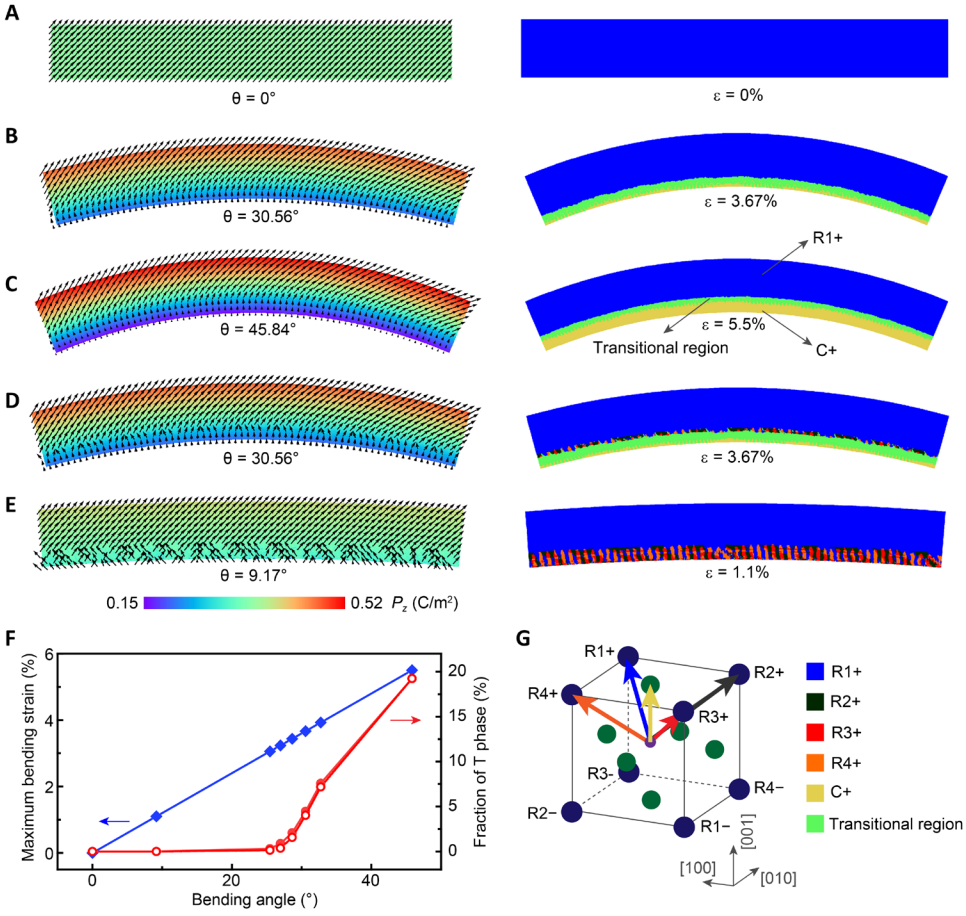

Fig. 4. Domain evolution of freestanding single-crystalline $BiFeO_3$ membrane during the bending or unbending process obtained by phase-field simulations. Snapshots of the corresponding *x*-*z* plane polarization vectors at the left column (where the color bar denotes the magnitude of the polarization) and their phase states or domain structures at the right column during the bending process of the $BiFeO_3$ membrane from the bending angle (**A**) θ = 0° (the initial state), (**B**) θ = 30.56°, to (**C**) θ = 45.84°, and the recovery process from θ = 45.84°, (**D**) θ = 30.56°, to (**E**) the final state θ = 9.17° during the unloading process. (**F**) Maximum strain and the fraction of tetragonal $BiFeO_3$ as a function of bending angle (θ) of the $BiFeO_3$ membrane for the loading (solid line) and unloading (dot) process. (**G**) Schematics of polarization directions of domains indicated in the right of (A) to (E).

boundary between T phase and R phase shifts downward as shown in the right panels of Fig. 4 (C to E), and the fraction of T phase (i.e., c+ domain) decreases as shown in Fig. 4F. The critical minimum bending angle for the formation of T phase is about 27.78°, and the corresponding critical minimum compressive strain (ε_{crit}) is about −3.33% from the simulated results, which is smaller than the previous results (ε_{crit}) reported (*18*) due to no-constraint or stress-free boundary conditions at the bottom of a freestanding $BiFeO_3$ membrane in our case. Last, when the membrane returns to the almost flat state with θ = 9.17° in Fig. 4F, the T phase disappears completely and only R domains exist, and the other types of R domains form because of the local ferroelastic (e.g., 71° or 109°) switching (fig. S6). It reveals that the freestanding $BiFeO_3$ membranes can be transformed reversibly between R phase and T phase.

DISCUSSION

$BiFeO_3$ is a typical ferroelectric/ferroelastic material, and it usually exhibits ferroelastic behavior and phase transition in response to strong mechanical stress. The elastic properties of strained $BiFeO_3$ thin film at the nanoscale were systematically studied by AFM-based technique, its Young's modulus softens during the R-T phase transition (*20*, *31*), and T phase is stiffer than R phase (*20*, *21*, *32*). Here, the elastic properties of freestanding $BiFeO_3$ membranes probably differ from those of the strained thin films. Fundamentally, both ferroelastic domain switching and phase transition are determined by the total energy (combination of elastic energy and electric energy). The most important difference between the strained $BiFeO_3$ film and freestanding $BiFeO_3$ membranes is the mechanical boundary condition (that is, additional elastic energy from the substrate clamping effect). This will induce a distinct energy profile under external mechanical and/or electrical stimuli. It has been demonstrated that by reducing the effective stress from the substrate clamping effect, large voltage-induced strain of about >10% was achieved in $BiFeO_3$ by phase transition (*5*). Moreover, the mobility of ferroelectric/ferroelastic domain walls could be enhanced in the declamped ferroelectric thin films (*33*, *34*). In our freestanding $BiFeO_3$ membranes, there is no substrate clamping effect; therefore, it is reasonable to expect much more elastic and flexible behavior in them from enhanced ferroelastic domain switching and improved strain tolerance, which is the same as we have demonstrated in our study. In addition, elastic properties, such as Young's modulus, are sensitive to both the phase and domain states, which means that they vary with the applied mechanical strain/stress (*35*). Hence, a full stress-strain curve is needed in the future to determine the true mechanical properties of the freestanding $BiFeO_3$ membranes.

We also notice some amount of residual strain that reaches ~1% after the application of the maximum bending strain (Fig. 3E), and it mainly originates from ferroelastic domain switching of rhombohedral $BiFeO_3$, as we demonstrated in Fig. 4E. Mechanical stress–induced irreversible ferroelastic domain switching is widely observed in a variety of ferroelectric/ferroelastic materials after releasing the applied stress (*35*). Here, the residual strain in freestanding $BiFeO_3$ membranes is about two times larger than that observed in conventional bulk ferroelectric/ferroelastic materials (*35*). Rhombohedral $BiFeO_3$ could probably tolerate a large spontaneous strain of about 7% in a single-domain state because it could maintain a large *c*/*a* ratio of about 1.07 (taking rhombohedral as pseudocubic for simplicity) (*18*). Because it turns to a multidomain state after ferroelastic domain switching (Fig. 4E), the residual strain from collective ferroelastic domain switching behavior will be smaller than the expected spontaneous strain from a single domain, as the internal stress will drive domain back-switching. In addition, as we mentioned above, freestanding $BiFeO_3$ membranes are fully declamped and irreversible/nonvolatile ferroelastic switching in $BiFeO_3$ could be stabilized (*14*). Nevertheless, a large residual strain stabilizes in freestanding $BiFeO_3$ membranes after irreversible ferroelastic domain switching.

This study, together with our previous report (*15*), demonstrates that flexibility and elastic behavior are distinct between the two-dimensional ferroelectric/ferroelastic membranes and their bulk materials, and it also indicates that the flexibility of the freestanding $BiFeO_3$ membranes will degrade with the increasing thickness. One critical factor is the defects, such as point defects and grain boundaries, which are well recognized to degrade the mechanical properties of ferroic oxides. The increase in thickness means the increase in epitaxial growth time. Because Bi is very volatile during high-temperature deposition, more and more defects will appear in the membranes. As a result, the mechanical strength will degrade in thicker $BiFeO_3$ membranes and they could crack easily (not shown here). Another important factor is the surface morphology or roughness, which becomes critical for thinner membranes. When the roughness is considerable to the length scale of the stress field or to the thickness of membranes, the surface/volume ratio increases a lot and the elastic behavior near the surface dominates, as revealed in nanowires (*10*). In our study, the surface is very smooth and the roughness is below 1 nm (Fig. 1E), which is two to three orders of magnitude smaller than the length scale of the bending stress. Therefore, we do not take surface morphology into consideration in this study, and superior flexibility could exist in relatively thicker membranes (fig. S7).

Besides, in this study, the bending of $BiFeO_3$ nanoribbon is along the in-plane [100] direction. To study how the elastic behavior depends on crystallographic orientations of bismuth ferrite, we compare the bending of the nanoribbon along the [110] direction by phase-field simulations (fig. S8). Compared to the domain structures for the bending along the [100] orientation, the stable domain structures become more complex (i.e., R1+, R4+, and R3+) for the bending along the [110] orientation, possibly arising from the complex coupling between the strain and polarization. A good elastic behavior (i.e., the bending angle under the same maximal bending strain) for the bending along the [110] orientation in the $BiFeO_3$ membrane is still kept because of the accommodation of complex domain structures and the R-T phase transition.

The mechanically induced R-T phase transition has been systematically studied in single-crystalline $BiFeO_3$ thin films and well demonstrated by x-ray diffraction, PFM, and TEM (*4*, *7*, *18*, *20*, *27*). Theoretically, it is an elastic energy–driven phase transition, occurring when the mechanical strain exceeds a critical value, (*18*), and phase-field simulations correlate well with experimental evidence in many previous reports (*7*, *18*, *20*, *27*). They introduced the mechanical strain discontinuously by lattice-mismatched substrates, and we introduced it continuously by bending; both could induce the R-T phase transition when the strain level exceeds a critical value. Our phase-field simulation indicates that a normal T phase, like that in $PbTiO_3$ with $(c/a - 1)$ <10%, is strong enough to tolerate a large bending strain of >5%. We can see that the freestanding $BiFeO_3$ membranes are still not breaking when the bending strain is >5%

(Fig. 3E and movie S3). Therefore, it is reasonable to expect that a super-tetragonal phase may further improve such super-elasticity and flexibility, as it could tolerate an even larger ferroelastic strain ($c/a - 1$) $\gg$ 10%.

Benefiting from the superior flexibility of freestanding single-crystalline $BiFeO_3$ membranes, large strain gradient could be easily achieved, which will be useful for macroscopic engineering of flexoelectricity (*28*). Here, the strain gradient along the thickness direction, which is inverse to the radius of curvature, could reach the level of 10^6 m^{-1} across the film thickness of >100 nm with the smallest radius of curvature of about 1 μm, and this is about five times magnitude larger than the traditional method by bending of bulk materials (*28*). Although a notable strain gradient of up to 10^{-5} to 10^{-6} m^{-1} was reported in the ferroic oxide thin film by strain engineering or nanoindentation, its length scale is usually limited to a few tens of nanometers because of the quick relaxation of strain/stress (*19*). Therefore, freestanding single-crystalline $BiFeO_3$ membranes with high flexibility provide a practical platform for flexoelectrics, extending their applications in flexible electronics. In addition, bending-induced phase transition in freestanding single-crystalline $BiFeO_3$ thin films will provide an alternative method to manipulate morphotropic phase boundaries irregardless of substrates, which is favorable for enhancing macroscopic dielectric, ferroelectric, and piezoelectric properties (*18*, *20*).

In conclusion, freestanding single-crystalline multiferroic $BiFeO_3$ membranes were fabricated by a lift-off process in water, and they exhibited high flexibility that is considerable to metallic and organic materials. A fundamental mechanism of such superior flexibility was proposed, and it is originated mainly from the reversible phase transition between the rhombohedral phase and the tetragonal phase in $BiFeO_3$. As polarization rotation and phase transition are general phenomena in many ferroic oxides, this study also implies that super-elasticity will exist in a variety of freestanding perovskite ferroic oxide membranes and related nanomaterials.

MATERIALS AND METHODS

Deposition of epitaxial thin films

At first, the polycrystalline $Sr_3Al_2O_6$ and $BiFeO_3$ targets were prepared by the solid-state reaction method. Both $Sr_3Al_2O_6$ and $BiFeO_3$ thin films were deposited sequentially on $SrTiO_3$(001) substrates by pulsed laser deposition using a KrF excimer laser with a wavelength of 248 nm. The $Sr_3Al_2O_6$ layer was grown at 740°C under an oxygen pressure of 15 Pa, the energy density was about ~0.8 J/cm^2, and the repetition rate was 5 Hz. The $BiFeO_3$ layer was grown at 600°C under an oxygen pressure of 1 Pa, the energy density was ~0.7 J/cm^2, and the repetition rate was 5 Hz. The $SrTiO_3/Sr_3Al_2O_6/BiFeO_3$ heterostructures were in situ annealed in the deposition chamber at 400°C for 30 min with an oxygen pressure of about 200 Pa.

Release and transfer $BiFeO_3$ membranes

A soft supporting layer was coated or attached to the surface of $BiFeO_3$ epitaxial thin films, and this supporting layer could be polydimethylsiloxane (PDMS), silicone-coated polyethylene terephthalate (PET), or photoresist (AR-P 3510T, Allresist GmbH). They were then immersed into deionized water at room temperature for a few hours, until $Sr_3Al_2O_6$ layer was completely dissolved and $BiFeO_3$ membrane was separated from the substrates. PDMS or PET could serve as flexible substrates. To transfer $BiFeO_3$ on the silicon substrate, "photoresist/$BiFeO_3$" stack was first transferred to Si and then the photoresist could be removed completely by acetone.

Structural electrical characterizations

High-resolution x-ray diffraction measurements (θ-2θ scan) were conducted with a PANalytical Empyrean diffractometer. The RSM was carried out by using high-resolution synchrotron x-ray, which was recorded at the BL09B beamline of the Shanghai Synchrotron Radiation Facility (SSRF). Atomic-resolution HAADF and annular bright-field images were obtained on a JEOL ARM200F microscope with CS-corrected STEM operated at 200 kV. In situ SEM bending test on $BiFeO_3$ nanoribbons was conducted by FIB (Helios NanoLab DualBeam) with Kleindiek mechanical manipulators. $BiFeO_3$ nanoribbons were fabricated from the large-area freestanding membrane using FIB (Ga+ sources, low ion current). The ferroelectric domains and polarization reversal behaviors were characterized by piezoresponse force microscopy (Asylum Cypher).

Phase-field simulations

In the phase-field model for the ferroelectric freestanding film, we use the local polarization vector $\mathbf{P} = (P_1, P_2, P_3)$ as the main order parameter, the spatial distribution of which describes ferroelectric domain structures. The temporal evolution of P_i (i = 1, 2, 3) in a (001)-oriented $BiFeO_3$ freestanding film is calculated by numerically solving the time-dependent Ginzburg-Landau equation (*36*)

$$\frac{\partial P_i(\mathbf{r},t)}{\partial t} = -L\frac{\delta F_{\text{tot}}}{\delta P_i(\mathbf{r},t)} \quad (1)$$

where $\mathbf{r}$ is the spatial position, L is a kinetic coefficient, and F_{tot} is the total free energy of the $BiFeO_3$ film, expressed as

$$F_{\text{tot}} = \iiint_{V_{\text{BFO}}} (f_{\text{land}} + f_{\text{elect}} + f_{\text{elastic}} + f_{\text{flexo}})\, dV \quad (2)$$

where V_{BFO} denotes the volume of the $BiFeO_3$ film and f_{land}, f_{elect}, f_{grad}, f_{elastic}, and f_{flexo} represent the local densities of landau, electrostatic, gradient, elastic, and flexoelectric energies, respectively. The mathematical expressions for the f_{land}, f_{elect}, f_{grad}, and f_{elastic} of the $BiFeO_3$ film are given in the literature (*7*, *27*–*30*, *37*). f_{flexo} can be given as

$$f_{\text{flexo}} = \frac{f_{ijkl}}{2}\left(\varepsilon_{ij}\frac{\partial P_k}{\partial x_1} - P_k\frac{\partial \varepsilon_{ij}}{\partial x_1}\right) \quad (3)$$

where f_{ijkl} (i, j, k, l = 1 to 3) denote the flexoelectric coupling coefficients (or flexovoltage coefficients) (*28*). In the simulation, Voigt notation of f_{ijkl} for the cubic symmetry is used, i.e., $f_{11} = f_{1111}$, $f_{12} = f_{1122}$, and $f_{44} = f_{1212}$. Because of the uncertainties of f_{ij}, f_{11} = 2.5 V, f_{12} = 2.5 V, and f_{44} = 1.25 V are used for the simulation.

Equation 1 can be solved numerically by a semi-implicit Fourier spectral method (*38*) based on a quasi–two-dimensional geometry sample on $800\Delta x \times 2\Delta y \times 126\Delta z$ with a real grid space of $\Delta x = \Delta y = \Delta z$ = 1 nm. The thickness of the film, the substrate, and the air are $110\Delta z$, $10\Delta z$, and $6\Delta z$, respectively. The mechanical boundary condition between the bottom layer of the film and the top layer of the substrate is set as a stress-free boundary to satisfy the boundary of the freestanding film.

SUPPLEMENTARY MATERIALS

Supplementary material for this article is available at http://advances.sciencemag.org/cgi/content/full/6/34/eaba5847/DC1

REFERENCES AND NOTES

1. H. U. Chung, B. H. Kim, J. Y. Lee, J. Lee, Z. Xie, E. M. Ibler, K. Lee, A. Banks, J. Y. Jeong, J. Kim, C. Ogle, D. Grande, Y. Yu, H. Jang, P. Assem, D. Ryu, J. W. Kwak, M. Namkoong, J. B. Park, Y. Lee, D. H. Kim, A. Ryu, J. Jeong, K. You, B. Ji, Z. Liu, Q. Huo, X. Feng, Y. Deng, Y. Xu, K.-I. Jang, J. Kim, Y. Zhang, R. Ghaffari, C. M. Rand, M. Schau, A. Hamvas, D. E. Weese-Mayer, Y. Huang, S. M. Lee, C. H. Lee, N. R. Shanbhag, A. S. Paller, S. Xu, J. A. Rogers, Binodal, wireless epidermal electronic systems with in-sensor analytics for neonatal intensive care. *Science* **363**, eaau0780 (2019).
2. S.-K. Kang, R. K. J. Murphy, S.-W. Hwang, S. M. Lee, D. V. Harburg, N. A. Krueger, J. Shin, P. Gamble, H. Cheng, S. Yu, Z. Liu, J. G. McCall, M. Stephen, H. Ying, J. Kim, G. Park, R. C. Webb, C. H. Lee, S. Chung, D. S. Wie, A. D. Gujar, B. Vemulapalli, A. H. Kim, K.-M. Lee, J. Cheng, Y. Huang, S. H. Lee, P. V. Braun, W. Z. Ray, J. A. Rogers, Bioresorbable silicon electronic sensors for the brain. *Nature* **530**, 71–76 (2016).
3. F. Li, M. J. Cabral, B. Xu, Z. X. Cheng, E. C. Dickey, J. M. LeBeau, J. L. Wang, J. Luo, S. Taylor, W. Hackenberger, L. Bellaiche, Z. Xu, L.-Q. Chen, T. R. Shrout, S. J. Zhang, Giant piezoelectricity of Sm-doped $Pb(Mg_{1/3}Nb_{2/3})O_3$-$PbTiO_3$ single crystals. *Science* **364**, 264–268 (2019).
4. J. X. Zhang, B. Xiang, Q. He, J. Seidel, R. J. Zeches, P. Yu, S. Y. Yang, C. H. Wang, Y. H. Chu, L. W. Martin, A. M. Minor, R. Ramesh, Large field-induced strains in a lead-free piezoelectric material. *Nat. Nanotechnol.* **6**, 98–102 (2011).
5. J. Zhang, X. Ke, G. Gou, J. Seidel, B. Xiang, P. Yu, W.-I. Liang, A. M. Minor, Y.-h. Chu, G. Van Tendeloo, X. Ren, R. Ramesh, A nanoscale shape memory oxide. *Nat. Commun.* **4**, 2768 (2013).
6. H. Pan, F. Li, Y. Liu, Q. Zhang, M. Wang, S. Lan, Y. Zheng, J. Ma, L. Gu, Y. Shen, P. Yu, S. Zhang, L.-Q. Chen, Y.-H. Lin, C.-W. Nan, Ultrahigh-energy density lead-free dielectric films via polymorphic nanodomain design. *Science* **365**, 578–582 (2019).
7. J. Ma, J. Ma, Q. Zhang, R. Peng, J. Wang, C. Liu, M. Wang, N. Li, M. Chen, X. Cheng, P. Gao, L. Gu, L.-Q. Chen, P. Yu, J. Zhang, C.-W. Nan, Controllable conductive readout in self-assembled, topologically confined ferroelectric domain walls. *Nat. Nanotechnol.* **13**, 947–952 (2018).
8. B. Wu, A. Heidelberg, J. J. Boland, Mechanical properties of ultrahigh-strength gold nanowires. *Nat. Mater.* **4**, 525–529 (2005).
9. S. Lee, A. Reuveny, J. Reeder, S. Lee, H. Jin, Q. Liu, T. Yokota, T. Sekitani, T. Isoyama, Y. Abe, Z. Suo, T. Someya, A transparent bending-insensitive pressure sensor. *Nat. Nanotechnol.* **11**, 472–478 (2016).
10. S. L. Wang, Z. W. Shan, H. Huang, The mechanical properties of nanowires. *Adv. Sci.* **4**, 1600332 (2017).
11. Y. Bitla, Y.-H. Chu, MICAtronics: A new platform for flexible X-tronics. *FlatChem* **3**, 26–42 (2017).
12. D. Lu, D. J. Baek, S. S. Hong, L. F. Kourkoutis, Y. Hikita, H. Y. Hwang, Synthesis of freestanding single-crystal perovskite films and heterostructures by etching of sacrificial water-soluble layers. *Nat. Mater.* **15**, 1255–1260 (2016).
13. D. Ji, S. Cai, T. R. Paudel, H. Sun, C. Zhang, L. Han, Y. Wei, Y. Zang, M. Gu, Y. Zhang, W. Gao, H. Huyan, W. Guo, D. Wu, Z. Gu, E. Y. Tsymbal, P. Wang, Y. Nie, X. Pan, Freestanding crystalline oxide perovskites down to the monolayer limit. *Nature* **570**, 87–90 (2019).
14. S. H. Baek, H. W. Jang, C. M. Folkman, Y. L. Li, B. Winchester, J. X. Zhang, Q. He, Y. H. Chu, C. T. Nelson, M. S. Rzchowski, X. Q. Pan, R. Ramesh, L. Q. Chen, C. B. Eom, Ferroelastic switching for nanoscale non-volatile magnetoelectric devices. *Nat. Mater.* **9**, 309–314 (2010).
15. G. Dong, S. Li, M. Yao, Z. Zhou, Y.-Q. Zhang, X. Han, Z. Luo, J. Yao, B. Peng, Z. Hu, H. Huang, T. Jia, J. Li, W. Ren, Z.-G. Ye, X. Ding, J. Sun, C.-W. Nan, L.-Q. Chen, J. Li, M. Liu, Super-elastic ferroelectric single-crystal membrane with continuous electric dipole rotation. *Science* **366**, 475–479 (2019).
16. A. Lai, Z. Du, C. L. Gan, C. A. Schuh, Shape memory and superelastic ceramics at small scales. *Science* **341**, 1505–1508 (2013).
17. M. Liu, T. Nan, J.-M. Hu, S.-S. Zhao, Z. Zhou, C.-Y. Wang, Z.-D. Jiang, W. Ren, Z.-G. Ye, L.-Q. Chen, N. X. Sun, Electrically controlled non-volatile switching of magnetism in multiferroic heterostructures *via* engineered ferroelastic domain states. *NPG Asia Mater.* **8**, e316 (2016).
18. R. J. Zeches, M. D. Rossell, J. X. Zhang, A. J. Hatt, Q. He, C.-H. Yang, A. Kumar, C. H. Wang, A. Melville, C. Adamo, G. Sheng, Y. H. Chu, J. F. Ihlefeld, R. Erni, C. Ederer, V. Gopalan, L. Q. Chen, D. G. Schlom, N. A. Spaldin, L. W. Martin, R. Ramesh, A strain-driven morphotropic phase boundary in $BiFeO_3$. *Science* **326**, 977–980 (2009).
19. Y. L. Tang, Y. L. Zhu, Y. Liu, Y. J. Wang, X. L. Ma, Giant linear strain gradient with extremely low elastic energy in a perovskite nanostructure array. *Nat. Commun.* **8**, 15994 (2017).
20. Q. Li, Y. Cao, P. Yu, R. K. Vasudevan, N. Laanait, A. Tselev, F. Xue, L. Q. Chen, P. Maksymovych, S. V. Kalinin, N. Balke, Giant elastic tunability in strained $BiFeO_3$ near an electrically induced phase transition. *Nat. Commun.* **6**, 8985 (2015).
21. P. Sharma, Y. Heo, B.-K. Jang, Y. Liu, V. Nagarajan, J. Li, C.-H. Yang, J. Seidel, Morphotropic phase elasticity of strained $BiFeO_3$. *Adv. Mater. Interfaces* **3**, 1600033 (2016).
22. M. Liu, B. M. Howe, L. Grazulis, K. Mahalingam, T. X. Nan, N. X. Sun, G. J. Brown, Voltage-impulse-induced non-volatile ferroelastic switching of ferromagnetic resonance for reconfigurable magnetoelectric microwave devices. *Adv. Mater.* **25**, 4886–4892 (2013).
23. Z. Y. Feng, H. S. Luo, Y. P. Guo, T. H. He, H. Q. Xu, Dependence of high electric-field-induced strain on the composition and orientation of $Pb(Mg_{1/3}Nb_{2/3})O_3$-$PbTiO_3$ crystals. *Solid State Commun.* **126**, 347–351 (2003).
24. M. I. Morozov, M. A. Einarsrud, J. R. Tolchard, P. T. Geiger, K. G. Webber, D. Damjanovic, T. Grande, In-situ structural investigations of ferroelasticity in soft and hard rhombohedral and tetragonal PZT. *J. Appl. Phys.* **118**, 164104 (2015).
25. K. G. Webber, M. Vögler, N. H. Khansur, B. Kaeswurm, J. E. Daniels, F. H. Schader, Review of the mechanical and fracture behavior of perovskite lead-free ferroelectrics for actuator applications. *Smart Mater. Struct.* **26**, 063001 (2017).
26. Y.-J. Li, J.-J. Wang, J.-C. Ye, X.-X. Ke, G.-Y. Gou, Y. Wei, F. Xue, J. Wang, C.-S. Wang, R.-C. Peng, X.-L. Deng, Y. Yang, X.-B. Ren, L.-Q. Chen, C.-W. Nan, J.-X. Zhang, Mechanical switching of nanoscale multiferroic phase boundaries. *Adv. Funct. Mater.* **25**, 3405–3413 (2015).
27. F. Xue, Y. Li, Y. Gu, J. Zhang, L.-Q. Chen, Strain phase separation: Formation of ferroelastic domain structures. *Phys. Rev. B* **94**, 220101 (2016).
28. B. Wang, Y. Gu, S. Zhang, L.-Q. Chen, Flexoelectricity in solids: Progress, challenges, and perspectives. *Prog. Mater. Sci.* **106**, 100570 (2019).
29. Y. Gu, Z. Hong, J. Britson, L.-Q. Chen, Nanoscale mechanical switching of ferroelectric polarization via flexoelectricity. *Appl. Phys. Lett.* **106**, 022904 (2015).
30. X. Lu, Z. Chen, Y. Cao, Y. Tang, R. Xu, S. Saremi, Z. Zhang, L. You, Y. Dong, S. Das, H. Zhang, L. Zheng, H. Wu, W. Lv, G. Xie, X. Liu, J. Li, L. Chen, L.-Q. Chen, W. Cao, L. W. Martin, Mechanical-force-induced non-local collective ferroelastic switching in epitaxial lead-titanate thin films. *Nat. Commun.* **10**, 3951 (2019).
31. Y. Cao, S. Yang, S. Jesse, I. Kravchenko, P. Yu, L.-Q. Chen, S. V. Kalinin, N. Balke, Q. Li, Exploring polarization rotation instabilities in super-tetragonal $BiFeO_3$ epitaxial thin films and their technological implications. *Adv. Electron. Mater.* **2**, 1600307 (2016).
32. Y. Heo, S. Hu, P. Sharma, K.-E. Kim, B.-K. Jang, C. Cazorla, C.-H. Yang, J. Seidel, Impact of isovalent and aliovalent doping on mechanical properties of mixed phase $BiFeO_3$. *ACS Nano* **11**, 2805–2813 (2017).
33. F. Griggio, S. Jesse, A. Kumar, O. Ovchinnikov, H. Kim, T. N. Jackson, D. Damjanovic, S. V. Kalinin, S. Trolier-McKinstry, Substrate clamping effects on irreversible domain wall dynamics in lead zirconate titanate thin films. *Phys. Rev. Lett.* **108**, 157604 (2012).
34. V. Nagarajan, A. Roytburd, A. Stanishevsky, S. Prasertchoung, T. Zhao, L. Chen, J. Melngailis, O. Auciello, R. Ramesh, Dynamics of ferroelastic domains in ferroelectric thin films. *Nat. Mater.* **2**, 43–47 (2003).
35. K. G. Webber, E. Aulbach, T. Key, M. Marsilius, T. Granzow, J. Roedel, Temperature-dependent ferroelastic switching of soft lead zirconate titanate. *Acta Mater.* **57**, 4614–4623 (2009).
36. Y. L. Li, S. Y. Hu, Z. K. Liu, L. Q. Chen, Effect of substrate constraint on the stability and evolution of ferroelectric domain structures in thin films. *Acta Mater.* **50**, 395–411 (2002).
37. R.-C. Peng, X. Cheng, J. Ma, H. Huang, J. Ma, L.-Q. Chen, C.-W. Nan, Understanding and predicting geometrical constraint ferroelectric charged domain walls in a $BiFeO_3$ island via phase-field simulations. *Appl. Phys. Lett.* **113**, 222902 (2018).
38. L. Q. Chen, J. Shen, Applications of semi-implicit Fourier-spectral method to phase field equations. *Comput. Phys. Commun.* **108**, 147–158 (1998).

Acknowledgments: We appreciate the support from the Jia-Lab for Interface and Atomic Structure. B.P. acknowledges technical support from S. Zhu for drawing the schematic illustrations. **Funding:** This work was supported by the National Key R&D Program of China (grants 2018YFB0407601, 2019YFA0307900, and 2016YFA0300702), the Natural Science Foundation of China (grants 11534015, 91964109, 51902248, 51902247, 51602244, 51802250, and 51802248), the National 111 Project of China (grant B14040), and the Key Research and Development Program of Shannxi (grant 2019TSLGY08-04) the China Postdoctoral Science Foundation (Grants 2019M663693 and 2019M663694) , Basic Research Program of Natural Science Foundation of Shannxi Province (Grant No. 2020JQ-059). Z. Luo acknowledges the financial support from the National Key R&D Program (2016YFA0300102) and the National Natural Science Foundation of China (11374010 and 11675179). X.C. and L.-Q.C. were supported as part of the Computational Materials Sciences Program, funded by the U.S. Department of Energy, Office of Science, Basic Energy Sciences, under award no. DE-SC0020145. Z.-G.Y. acknowledges support from the Natural Sciences and Engineering Research Council of Canada (NSERC; grant no. 203773). **Author contributions:** B.P., Z.Z., and M.L. initialized the idea and designed the experiment. B.P. and R.Q. fabricated thin films and membranes. Y.-Q.Z. and G.D. conducted STEM and the in situ SEM bending experiments under the guidance of Z.S. R.-C.P., X.C., and F.X. carried out the phase-field simulation under the guidance of L.-Q.C. Y.Z. conducted the PFM tests under the guidance of T.L. and T.M. Z. Liu conducted the RSM tests under the guidance of Z. Luo B.P. and R.-C.P. wrote the draft. M.L. and Z.Z. supervised the project. S.W. and Y.X. contributed to the discussion during revision. Z.H.,

W.R., and Z.-G.Y. contributed to the interpretation of the experimental results. All authors contributed to the discussion of the results and the revision of the manuscript. **Competing interests:** The authors declare that they have no competing interests. **Data and materials availability:** All data needed to evaluate the conclusions in the paper are present in the paper and/or the Supplementary Materials. Additional data related to this paper may be requested from the authors. The domain structures and polarization vectors can be provided by the corresponding author (M.L.), pending scientific review, and a completed material transfer agreement. Requests for the domain structures and polarization vectors should be submitted to mingliu@xjtu.edu.cn (Xi'an Jiaotong University).

Submitted 19 December 2019
Accepted 10 July 2020
Published 21 August 2020
10.1126/sciadv.aba5847

Citation: B. Peng, R.-C. Peng, Y.-Q. Zhang, G. Dong, Z. Zhou, Y. Zhou, T. Li, Z. Liu, Z. Luo, S. Wang, Y. Xia, R. Qiu, X. Cheng, F. Xue, Z. Hu, W. Ren, Z.-G. Ye, L.-Q. Chen, Z. Shan, T. Min, M. Liu, Phase transition enhanced superior elasticity in freestanding single-crystalline multiferroic $BiFeO_3$ membranes. *Sci. Adv.* **6**, eaba5847 (2020).

Science Advances

Phase transition enhanced superior elasticity in freestanding single-crystalline multiferroic $BiFeO_3$ membranes

Bin Peng, Ren-Ci Peng, Yong-Qiang Zhang, Guohua Dong, Ziyao Zhou, Yuqing Zhou, Tao Li, Zhijie Liu, Zhenlin Luo, Shaohao Wang, Yan Xia, Ruibin Qiu, Xiaoxing Cheng, Fei Xue, Zhongqiang Hu, Wei Ren, Zuo-Guang Ye, Long-Qing Chen, Zhiwei Shan, Tai Min and Ming Liu

Sci Adv **6** (34), eaba5847.
DOI: 10.1126/sciadv.aba5847